Journal of the Optical Society of America B
OPTICAL PHYSICS

Inverse-designed broadband meta-coupler with high efficiency on thin-film lithium niobate

ZHIWEI WEI,[1] JIANGWEI WU,[1] CHENGYU CHEN,[1] WENJIE WAN,[1,2] YUPING CHEN,[1,*] AND XIANFENG CHEN[1,3]

[1]State Key Laboratory of Advanced Optical Communication Systems and Networks, School of Physics and Astronomy, Shanghai Jiao Tong University, Shanghai 200240, China
[2]University of Michigan Shanghai Jiao Tong University Joint Institute, Shanghai Jiao Tong University, Shanghai, China
[3]Collaborative Innovation Center of Light Manipulations and Applications, Shandong Normal University, Jinan 250358, China
*ypchen@sjtu.edu.cn

Received 17 October 2024; revised 9 January 2025; accepted 14 January 2025; posted 14 January 2025; published 18 February 2025

Efficiently coupling free-space light with a large bandwidth to arbitrary positions in on-chip systems is a significant challenge. In this work, we address this issue by utilizing an inverse-designed metasurface as a meta-coupler, replacing conventional grating couplers. Our meta-coupler achieved a maximum coupling efficiency of 90% (−0.46 dB). The 1-dB bandwidth spans 138 nm (1450–1588 nm), while the 3-dB bandwidth extends over 300 nm (1425–1725 nm), far exceeding the bandwidth of traditional grating couplers used on thin-film lithium niobate. This meta-coupler demonstrates strong potential for on-chip systems requiring multi-wavelength interactions, such as integrated lasers and amplifiers.

https://doi.org/10.1364/JOSAB.545358

1. INTRODUCTION

Thin-film lithium niobate (LN) is a widely used platform for integrated optics due to its excellent optical properties such as a relatively large refractive index and large transparency window, as well as electro-optic, acousto-optic, photorefractive, piezoelectric, and other nonlinear optical properties [1]. Many applications based on thin-film LN have been demonstrated, such as optical frequency combs [2,3], electro-optical modulators [4,5], wavelength converters [6,7], sensors [8–10], optical phased array [11], and on-chip lasers [12–14]. A coupler is a basic element of an on-chip photonic system. An efficient coupler is essential to realize a high-performance on-chip photonic device. At present, there are two common coupling approaches: edge coupler and grating coupler [15,16]. An edge coupler has the characteristics of relatively low loss, large bandwidth, low polarization dependence, low placement flexibility, and the need for end-facet dicing and polishing. The grating coupler has the characteristics of relatively high loss, small bandwidth, high polarization dependence, and high placement flexibility. The couplers currently used for on-chip lasers and amplifiers [17] have low placement flexibility and are restricted to the edges or corners of the chip, which reduces the system's integration and the chip's utilization. It is challenging to efficiently couple free-space light with multiple wavelengths to the arbitrary position of the on-chip system, involving the interaction of multiple wavelengths, such as on-chip lasers and amplifiers. Metasurfaces can manipulate the amplitude, phase, polarization, and frequency of light, which provides the opportunity to solve the problem of multi-wavelength coupling [18,19]. Recently, phase-gradient metasurfaces used as meta-couplers have been demonstrated [20–25]. However, the coupling efficiency is relatively low. In contrast to the forward design method with a limited parameter space, the inverse design method based on intelligent algorithms provides comprehensive optimization. A series of applications based on the inverse design method have been demonstrated recently, such as metalenses [26,27], optical splitters [28–30], reflectors [31,32], couplers [33,34], waveguide crossings [35], optical filters [36], optical diodes [37], resonators [32], and second-harmonic generation [38].

We proposed an inverse-designed broadband meta-coupler with high coupling efficiency (CE) on thin-film LN to efficiently couple broadband free-space light to the arbitrary position of the on-chip system. First, based on generalized Snell's law, a meta-coupler for 1550 nm was designed. Then, by inverse design, a meta-coupler for 1460 and 1550 nm was realized. Without inverse design, the coupling efficiency for 1460/1550 nm is 32%/85%. With inverse design, the coupling efficiency for 1460/1550 nm is 77%/83%, with a 3-dB bandwidth of 300 nm and a 1-dB bandwidth of 138 nm, and the maximum efficiency is 90% (−0.46 dB). To the best of our knowledge, compared to the grating coupler, the biggest bandwidth is demonstrated in our work, which shows the potential application for on-chip systems involving the interaction of multiple wavelengths, such as on-chip lasers and amplifiers.

2. THEORY

An on-chip broadband meta-coupler on thin-film LN was demonstrated by inverse design. Figure 1 shows a schematic illustration of the meta-coupler. The design process can be divided into two steps to decrease iteration times and improve meta-coupler efficiency. First, based on the generalized Snell's law [39],

$$n_t \sin\theta_t - n_i \sin\theta_i = \frac{\lambda_0}{2\pi}\frac{d\phi}{dx}, \tag{1}$$

$$\sin\theta_r - \sin\theta_i = \frac{\lambda_0}{2\pi n_i}\frac{d\phi}{dx}. \tag{2}$$

A phase-gradient amorphous silicon ($\alpha - \mathrm{Si}$) metasurface on the thin-film LN was designed as a meta-coupler for efficient coupling at 1550 nm. Here, θ_t/θ_i is the angle of refraction/reflection, n_t/n_i is the corresponding refractive index, λ_0 is the vacuum wavelength, and $\frac{d\phi}{dx}$ is the phase gradient between neighboring antennas. Here, the incident angle θ_i is 5 deg, and n_i is 1. The period P of the unit of metasurface is 500 nm, and the height H of the unit of metasurface is 945 nm. dx is 500 nm. The footprint of the meta-coupler is 3 μm × 3 μm. According to Eq. (2), a proper phase gradient $d\phi$ is designed, and we let $\frac{\lambda_0}{2\pi n_i}\frac{d\phi}{dx} + \sin\theta_i > 1 > \sin\theta_r$. Then the reflected beam becomes evanescent. Generally, for guided waves in the thin-film LN waveguide, the effective refractive index n_{eff} is $n_t \sin\theta_t$, and only several limited values of θ_t are allowed in the waveguide. A proper phase gradient is needed to satisfy Eq. (1) to realize efficient coupling. Considering these conditions, we designed a meta-coupler to efficiently couple the free-space light with a wavelength of 1550 nm to the thin-film LN waveguide. Figure 1(a) shows a schematic diagram of the meta-coupler principle on thin-film lithium niobate. Most of the free-space light was coupled into thin-film LN through an $\alpha - \mathrm{Si}$ meta-coupler. Here, a Z-cut thin-film LN with a thickness of 600 nm was used, and the 2-μm-thick $\mathrm{SiO_2}$ beneath the meta-coupler was corroded to improve the efficiency. The unit of metasurface is shown in Fig. 1(b). The meta-coupler on thin-film LN without inverse design is shown in Fig. 1(c). The meta-coupler on thin-film LN with inverse design is shown in Fig. 1(d). There were two air holes on either side of the waveguide, which were used to corrode the silica beneath the meta-coupler. Figure 1(e) shows an enlarged view of the meta-coupler without inverse design. Figure 1(f) shows an enlarged view of the meta-coupler with inverse design. Figure 1(g) shows the cross-section diagram of the meta-coupler on thin-film LN. Considering that the value of $d\phi$ is positive, the light coupled into the waveguide will propagate along the positive X axis. Then, the $d\phi$ and the initial phase retardation ϕ_0 of the transmitted light due to the first antenna were swept. The range of the $d\phi$ and the initial phase retardation ϕ_0 is 2π.

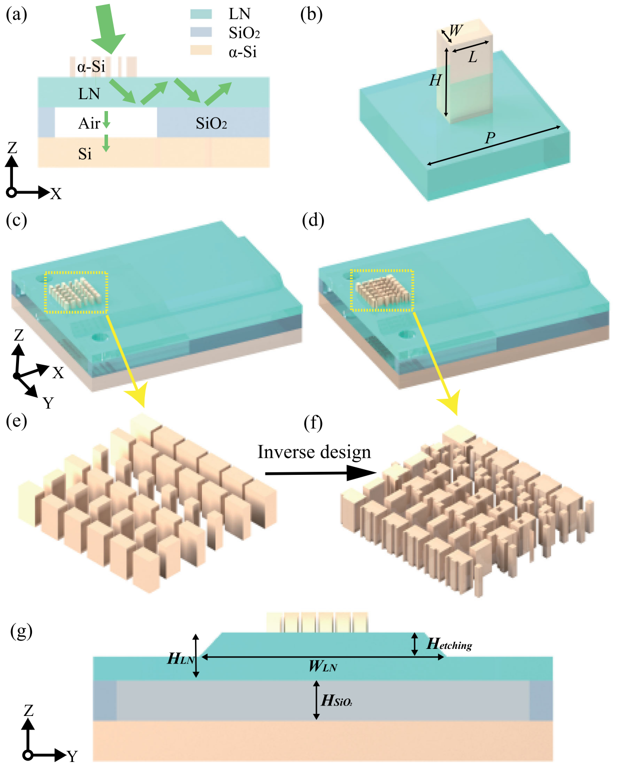

Fig. 1. Schematic illustration of the compact broadband meta-coupler by inverse design. (a) Schematic diagram of the principle of the meta-coupler. (b) Unit of the metasurface. (c) Meta-coupler on thin-film LN without inverse design. (d) Meta-coupler on thin-film LN with inverse design. (e) Enlarged view of the meta-coupler without inverse design. (f) Enlarged view of the meta-coupler with inverse design. (g) Cross-section diagram of the meta-coupler on thin-film LN.

Second, the meta-coupler for efficient coupling at 1550 nm was used as the initial condition of the inverse design. The objective function is given by

$$\text{Maximize } \eta_{\lambda 1550} \times \eta^2_{\lambda 1460}, \tag{3}$$

where $\eta_{\lambda 1550}$ is the efficiency of light at a wavelength of 1550 nm and $\eta^2_{\lambda 1460}$ is the efficiency of light at a wavelength of 1460 nm. The size of the unit of inverse design is 100 nm × 100 nm × 945 nm. The material of the unit is air or $\alpha - \mathrm{Si}$. The genetic algorithm (GA) was used for inverse design. The code of the GA was written in Python. The generation in the GA was set to 20. The population in the GA was set to 60. The optical simulation is based on the finite-different time-domain (FDTD) method. The light source was a total-field scattered-field (TFSF) light source [40], which was commonly used to analyze antenna-scattering attributes and calculate device coupling efficiency [21]. The boundary condition was set as a perfect matching layer.

3. RESULTS AND DISCUSSION

Figure 2(a) shows the relation between the phase retardation of the transmitted light and the geometry (L, W) of the unit of the meta-coupler. Figure 2(b) shows the relation between the transmittance of the transmitted light and the geometry (L, W) of the unit of the meta-coupler. The phase map was used in our design. Based on experimental results, the height H of the unit is set to 945 nm, ensuring that the phase range $(-\pi, \pi)$ is large enough. The $\alpha - \mathrm{Si}$ was prepared by plasma-enhanced chemical vapor deposition (PECVD). Then, the data of the refractive index of $\alpha - \mathrm{Si}$ are measured by a spectroscopic ellipsometry analyzer (SEA). The incident light is a TE wave. The

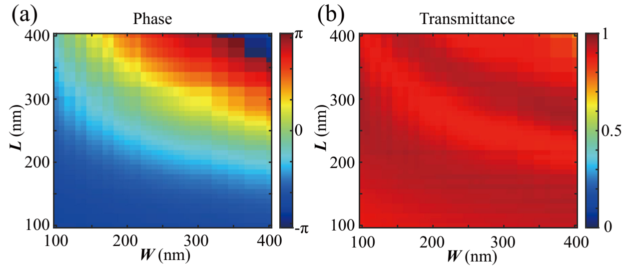

Fig. 2. (a) Relation between the phase retardation of the transmitted light and the geometry (L, W) of the unit of the metasurface. (b) Relation between the phase retardation of the transmitted light and the geometry (L, W) of the unit of the metasurface.

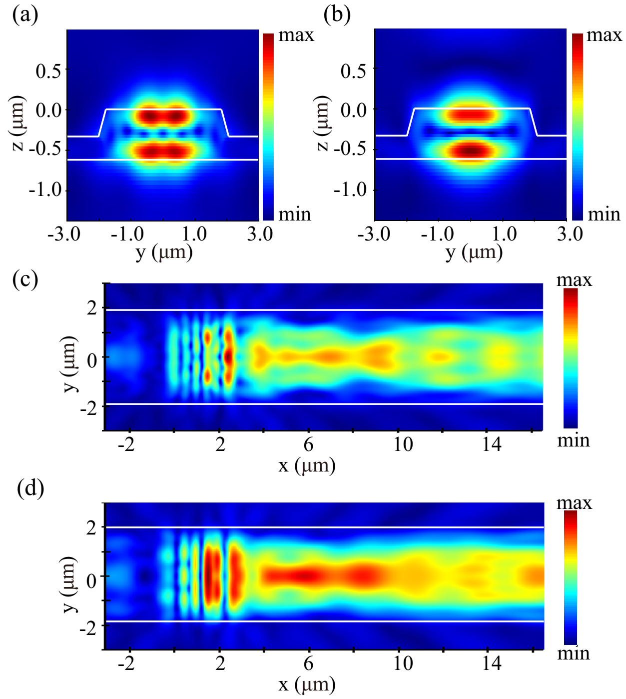

Fig. 3. $|E|$ distribution under TE plane wave illumination. (a) $|E|$ distribution in the $y-z$ plane under TE plane wave illumination ($\lambda = 1.46$ μm). The waveguide profile is marked with white solid lines. (b) $|E|$ distribution in the $y-z$ plane under TE plane wave illumination ($\lambda = 1.55$ μm). (c) $|E|$ distribution in the $x-y$ plane under TE plane wave illumination ($\lambda = 1.46$ μm). (d) $|E|$ distribution in the $x-y$ plane under TE plane wave illumination ($\lambda = 1.55$ μm).

polarization direction is along the y direction. The thickness of LN is 600 nm. The etching depth is 350 nm. The width of the waveguide is 3.8 μm. Figure 3 shows the $|E|$ distribution with inverse design in thin-film LN. The $|E|$ distribution in the $y-z$ plane under TE plane wave illumination ($\lambda = 1.46$ μm) is shown in Fig. 3(a). The waveguide profile is marked with solid white lines. The $|E|$ distribution in the $x-y$ plane under TE plane wave illumination ($\lambda = 1.55$ μm) is shown in Fig. 3(b). The mode profile at 1460 nm is close to TE_{11}, and the mode profile at 1550 nm is close to TE_{01}. The $|E|$ distribution in the $x-y$ plane under TE plane wave illumination ($\lambda = 1.46$ μm) is shown in Fig. 3(c). The waveguide profile is marked with solid white lines. The $|E|$ distribution in the $x-y$ plane under TE plane wave illumination ($\lambda = 1.55$ μm) is shown in Fig. 3(d). From Figs. 3(c) and 3(d), we find that most of the light propagates along the positive X axis, which agrees with our theory. To investigate the influence of the polarization of the incident light, the polarization of the incident light was set to TM polarization. Figure 4 shows the $|E|$ distribution with inverse design in thin-film LN under TM plane wave illumination. The $|E|$ distribution in the $y-z$ plane under TM plane wave illumination ($\lambda = 1.46$ μm) is shown in Fig. 4(a). The waveguide profile is marked with solid white lines. The $|E|$ distribution in the $x-y$ plane under TM plane wave illumination ($\lambda = 1.55$ μm) is shown in Fig. 4(b). The $|E|$ distribution in the $x-y$ plane under TM plane wave illumination ($\lambda = 1.46$ μm) is shown in Fig. 4(c). The $|E|$ distribution in the $x-y$ plane under TM plane wave illumination ($\lambda = 1.55$ μm) is shown in Fig. 4(d). Figure 5 shows the coupling efficiency (CE) of the meta-coupler with(out) inverse design. The efficiency of the meta-coupler with inverse design under TE plane wave illumination is plotted in black, and the efficiency of the meta-coupler without inverse design under TE plane wave illumination is plotted in cyan. The efficiency of the meta-coupler without inverse design under TM plane wave illumination is plotted in red. The efficiency of the meta-coupler without inverse design under TM plane wave illumination is plotted in green. The data at a wavelength of 1460 nm are marked with green points, and the data at a wavelength of 1550 nm are marked with yellow points. Without inverse design, the coupling efficiency at 1460/1550 nm under TE plane wave illumination is 32%/85%, and with inverse design, the coupling efficiency at 1460/1550 nm under TE plane wave illumination is 77%/83%. The coupling efficiency at 1460/1550 nm under TE plane wave illumination is much higher than the coupling efficiency at 1460/1550 nm under TM plane wave illumination. In the simulation to find the relation between the phase retardation of the transmitted light and the geometry of the unit of the meta-coupler, the polarization of the incident light was set as TE. During the forward design, the incident light was set as TE. So, the device is designed for the TE mode. For the TM mode, the phase response of the metasurface is different, which may not satisfy the conditions of Eq. (1), so the coupling efficiency is low and uncertain. After the inverse design for the TE mode, the polarization was changed to TM to find the polarization sensitivity. And the result shows that the structure is sensitive to polarization. After the inverse design, the coupling efficiency at 1460 nm under TE plane wave illumination can be increased by 141%, while the coupling efficiency at 1550 nm is almost the same. After the inverse design, the maximum CE under TE plane wave illumination is 86%. The 1-dB bandwidth is 138 nm from 1450 to 1588 nm, and the 3-dB bandwidth is 300 nm from 1425 to 1725 nm. S(short), C(conventional), and L(long) bands are commonly used in optical communication. In Fig. 5, the S/C/L bands are highlighted by translucent yellow/purple/red areas, respectively. The S band and C band are within the 1-dB bandwidth. The L band is within the 3-dB bandwidth. Our meta-coupler can work in the S, C, and L bands.

To further investigate the influence of different parameters of the meta-coupler on the thin-film LN waveguide, the width W_{LN}, the etching depth, the thickness H_{LN} of the thin-film LN waveguide, and the fabrication error of the meta-coupler were

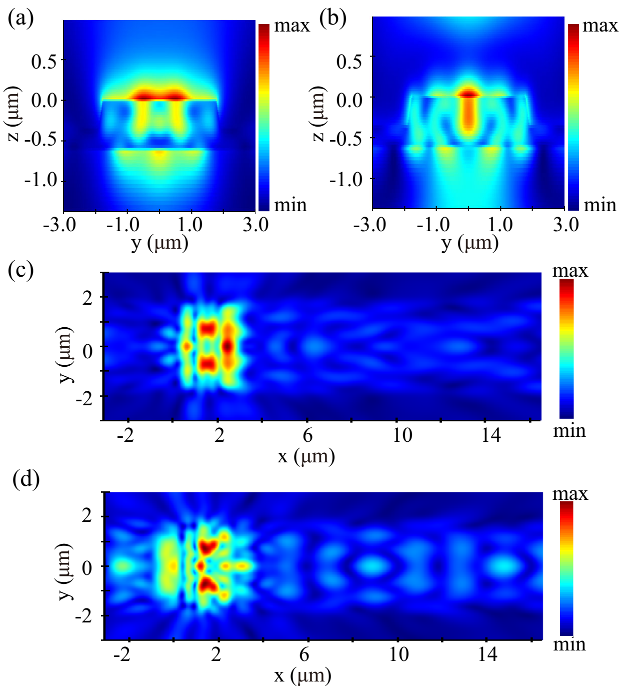

Fig. 4. $|E|$ distribution under TM plane wave illumination. (a) $|E|$ distribution in the $y-z$ plane under TM plane wave illumination ($\lambda = 1.46\ \mu\text{m}$). The waveguide profile is marked with solid white lines. (b) $|E|$ distribution in the $y-z$ plane under TM plane wave illumination ($\lambda = 1.55\ \mu\text{m}$). (c) $|E|$ distribution in the $x-y$ plane under TM plane wave illumination ($\lambda = 1.46\ \mu\text{m}$). (d) $|E|$ distribution in the $x-y$ plane under TM plane wave illumination ($\lambda = 1.55\ \mu\text{m}$).

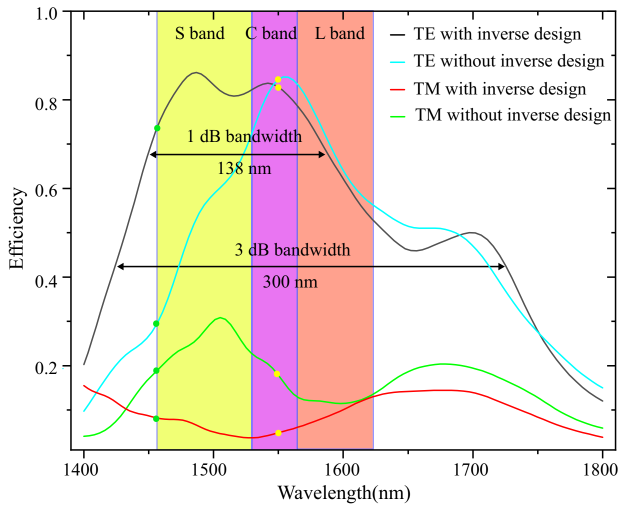

Fig. 5. Efficiency of the meta-coupler with(out) inverse design. The efficiency of the meta-coupler with inverse design under TE plane wave illumination is plotted in black. The efficiency of the meta-coupler without inverse design under TE plane wave illumination is plotted in cyan. The efficiency of the meta-coupler with inverse design under TM plane wave illumination is plotted in red. The efficiency of the meta-coupler without inverse design under TM plane wave illumination is plotted in green. The data at a wavelength of 1460 nm are marked with green points, and the data at a wavelength of 1550 nm are marked with yellow points. The S(short)/C(conventional)/L(long) bands are highlighted by translucent yellow/purple/red areas, respectively.

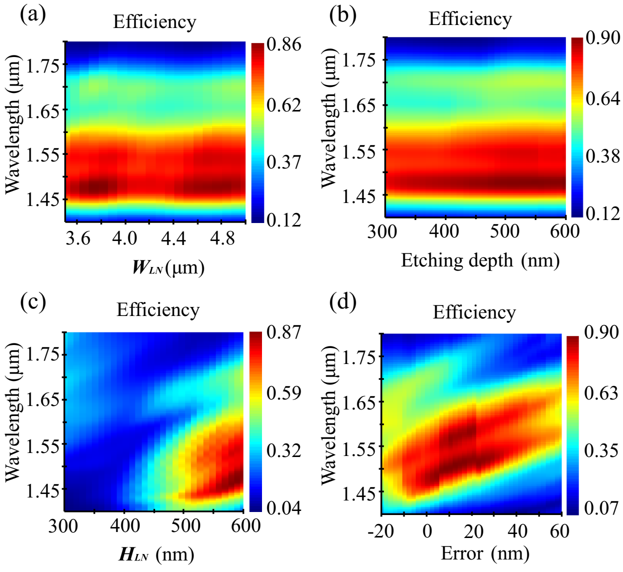

Fig. 6. Influence of the width W_{LN}, etching depth, thickness H_{LN}, and fabrication error of LN waveguide. (a) The efficiency map as a function of wavelength and W_{LN}. (b) The efficiency map as a function of wavelength and etching depth. (c) The efficiency map as a function of wavelength and thickness H_{LN}. (d) The efficiency map as a function of wavelength and fabrication error.

adjusted. The influence of the width W_{LN} of the thin-film LN waveguide, with a thickness of 600 nm and an etching depth of 350 nm, is shown in Fig. 6(a). The maximum CE at 1460 nm is 82% when W_{LN} is 3.74 μm. The maximum CE at 1550 nm is 80% when W_{LN} is 4.68 μm. The maximum CE is 86% when the wavelength is 1480 nm and W_{LN} is 3.74 μm. The influence of the width W_{LN} of the thin-film LN waveguide is relatively small, which shows an excellent fabrication tolerance. The influence of the etching depth of the thin-film LN waveguide with a thickness of 600 nm and a width of 3.8 μm is shown in Fig. 6(b). The maximum CE at 1460 nm is 85% when the etching depth is 600 nm. The maximum CE at 1550 nm is 83% when the etching depth is 528 nm. The maximum CE is 90% when the wavelength is 1480 nm and the etching depth is 600 nm. The results show that increasing the etching depth helps improve the CE. The influence of the thickness H_{LN} of the thin-film LN waveguide, with a width of 3.8 μm and an etching depth of 300 nm, is shown in Fig. 6(c). The maximum CE at 1460 nm is 86% when H_{LN} is 579 nm. The maximum CE at 1550 nm is 78% when H_{LN} is 579 nm. The maximum CE is 87% when the wavelength is 1469 nm and H_{LN} is 590 nm. The results show that increasing the thickness helps improve the CE. The influence of the fabrication error of the meta-coupler is shown in Fig. 6(d), while the thin-film LN waveguide has a thickness of 600 nm, a width of 3.8 μm, and an etching depth of 350 nm. The meta-coupler with a fabrication error of 20 nm means that the width and length of all the structures in the meta-coupler increase by 20 nm. When the fabrication error varies from −10 to 48 nm, the CE at a wavelength of 1550 nm ranges from 70% to 85%. The meta-coupler shows an excellent fabrication tolerance.

Table 1. Comparison of Grating Coupler on Thin-Film Lithium Niobate

			CE (dB)		3-dB Bandwidth (nm)		1-dB Bandwidth (nm)	
Reference	Inverse Design	Reflector	Sim	Exp	Sim	Exp	Sim	Exp
[41]	No	No	−2.7	−3.06		102		55
[42]	No	No	−2	−3.6	44	48		
[43]	No	Yes	−3.13	−3.5				
[44]	No	Yes	−0.51	−1.43	38			
[45]	No	No	−4.57	−5.82	61	57		
[46]	No	No	−2.98	−3.58			58	
[47]	No	No	−3	−3.27		35		
[48]	No	No	−3.21	−4.02		70		
[49]	Yes	Yes	−0.71	−0.89			46	45
[50]	No	No	−1.40	−2.20	47	86		
[51]	Yes	No	−2					
[52]	Yes	No	−2.75	−3.37		75		
[53]	Yes	No	−2.98	−3.8	86	∼ 120	46	71.4
This work	Yes	No	−0.46		300		138	

A coupler is a basic element of an on-chip photonic system. An efficient coupler is essential to realize a high-performance on-chip photonic device. The functionality of our work is similar to that of the grating coupler, which can couple the free-space light into the arbitrary position of the on-chip system. A comparison of grating couplers on thin-film lithium niobate is shown in Table 1. This work breaks the limited bandwidth of the grating coupler. High efficiency and ultra-large bandwidth were realized. There are several important details for realizing a meta-coupler with high coupling efficiency and large bandwidth. First, the SiO_2 beneath the meta-coupler is corroded to increase the refractive index contrast. Thereby, more light is limited in the LN, improving the coupling efficiency. Second, the phase-gradient metasurface was used as a meta-coupler, and by inverse design, the dispersion of the meta-coupler was optimized, improving the bandwidth of the meta-coupler.

Funding. National Natural Science Foundation of China (12134009, 12474335).

Acknowledgment. We acknowledge the Center for Advanced Electronic Materials and Devices (AEMD) of Shanghai Jiao Tong University for the fabrication support.

Disclosures. The authors declare no conflicts of interest.

Data availability. Data underlying the results presented in this paper are not publicly available at this time but may be obtained from the authors upon reasonable request.

REFERENCES

1. Y. Qi and Y. Li, “Integrated lithium niobate photonics,” Nanophotonics **9**, 1287–1320 (2020).
2. C. Wang, M. Zhang, M. Yu, *et al.*, “Monolithic lithium niobate photonic circuits for Kerr frequency comb generation and modulation,” Nat. Commun. **10**, 978 (2019).
3. Y. He, Q.-F. Yang, J. Ling, *et al.*, “Self-starting bi-chromatic $LiNbO_3$ soliton microcomb,” Optica **6**, 1138–1144 (2019).
4. C. Wang, M. Zhang, X. Chen, *et al.*, “Integrated lithium niobate electro-optic modulators operating at CMOS-compatible voltages,” Nature **562**, 101–104 (2018).
5. Y. Xue, R. Gan, K. Chen, *et al.*, “Breaking the bandwidth limit of a high-quality-factor ring modulator based on thin-film lithium niobate,” Optica **9**, 1131–1137 (2022).
6. Z. Hao, L. Zhang, W. Mao, *et al.*, “Second-harmonic generation using d_{33} in periodically poled lithium niobate microdisk resonators,” Photonics Res. **8**, 311–317 (2020).
7. J. Lu, J. B. Surya, X. Liu, *et al.*, “Periodically poled thin-film lithium niobate microring resonators with a second-harmonic generation efficiency of 250,000%/w,” Optica **6**, 1455–1460 (2019).
8. X. Wang, J. Wu, C. Chen, *et al.*, “Enhanced sensing resolution with microcavity mode oscillation generated by thermal-optic and photorefractive nonlinearity,” Appl. Phys. Lett. **124**, 061108 (2024).
9. X. Wang, T. Yuan, J. Wu, *et al.*, “Enhanced temperature sensing by multi-mode coupling in an on-chip microcavity system,” Laser Photonics Rev. **18**, 2300760 (2024).
10. T. Yuan, X. Wang, J. Wu, *et al.*, “Frequency-space selective Fano resonance based on a micro-ring resonator on lithium niobate on insulator,” Laser Photonics Rev. **18**, 2400457 (2024).
11. J. Wu, Z. Liang, X. Wang, *et al.*, “End-fire optical phased array for passive beam steering on thin-film lithium niobate,” Opt. Lett. **49**, 5087–5090 (2024).
12. Y. Liu, X. Yan, J. Wu, *et al.*, “On-chip erbium-doped lithium niobate microcavity laser,” Sci. China Phys. Mech. Astron. **64**, 234262 (2021).
13. V. Snigirev, A. Riedhauser, G. Lihachev, *et al.*, “Ultrafast tunable lasers using lithium niobate integrated photonics,” Nature **615**, 411–417 (2023).
14. J. Wu, X. Yan, X. Wang, *et al.*, “Efficient integrated amplifier-assisted laser on erbium-doped lithium niobate,” ACS Photonics **11**, 2114–2122 (2024).
15. L. Cheng, S. Mao, Z. Li, *et al.*, “Grating couplers on silicon photonics: design principles, emerging trends and practical issues,” Micromachines **11**, 666 (2020).
16. X. Mu, S. Wu, L. Cheng, *et al.*, “Edge couplers in silicon photonic integrated circuits: a review,” Appl. Sci. **10**, 1538 (2020).
17. Q. Luo, F. Bo, Y. Kong, *et al.*, “Advances in lithium niobate thin-film lasers and amplifiers: a review,” Adv. Photonics **5**, 034002 (2023).
18. A. I. Kuznetsov, M. L. Brongersma, J. Yao, *et al.*, “Roadmap for optical metasurfaces,” ACS Photonics **11**, 816–865 (2024).
19. S. A. Schulz, R. F. Oulton, M. Kenney, *et al.*, “Roadmap on photonic metasurfaces,” Appl. Phys. Lett. **124**, 260701 (2024).
20. Y. Chen, X. Zheng, X. Zhang, *et al.*, “Efficient meta-couplers squeezing propagating light into on-chip subwavelength devices in a controllable way,” Nano Lett. **23**, 3326–3333 (2023).
21. Y. Meng, Z. Liu, Z. Xie, *et al.*, “Versatile on-chip light coupling and (de) multiplexing from arbitrary polarizations to controlled waveguide modes using an integrated dielectric metasurface,” Photonics Res. **8**, 564–576 (2020).
22. D. Gu, C. Liang, L. Sun, *et al.*, “Optical metasurfaces for waveguide couplers with uniform efficiencies at RGB wavelengths,” Opt. Express **29**, 29149–29164 (2021).

23. Y. Guo, M. Pu, X. Li, *et al.*, "Chip-integrated geometric metasurface as a novel platform for directional coupling and polarization sorting by spin–orbit interaction," IEEE J. Sel. Top. Quantum Electron. **24**, 1–7 (2018).
24. Y. Zhang, Z. Li, W. Liu, *et al.*, "Spin-selective and wavelength-selective demultiplexing based on waveguide-integrated all-dielectric metasurfaces," Adv. Opt. Mater. **7**, 1801273 (2019).
25. X. Li, G. Cheng, D. X. Yan, *et al.*, "One-dimensional terahertz dielectric gradient metasurface for broadband spoof surface plasmon polaritons couplers," Opt. Lett. **46**, 290–293 (2021).
26. R. Pestourie, C. Pérez-Arancibia, Z. Lin, *et al.*, "Inverse design of large-area metasurfaces," Opt. Express **26**, 33732–33747 (2018).
27. Z. Li, R. Pestourie, J.-S. Park, *et al.*, "Inverse design enables large-scale high-performance meta-optics reshaping virtual reality," Nat. Commun. **13**, 1–11 (2022).
28. Y. Xie, T. Huang, Q. Ji, *et al.*, "Design of an arbitrary ratio optical power splitter based on a discrete differential multiobjective evolutionary algorithm," Appl. Opt. **59**, 1780–1785 (2020).
29. A. Y. Piggott, E. Y. Ma, L. Su, *et al.*, "Inverse-designed photonics for semiconductor foundries," ACS Photonics **7**, 569–575 (2020).
30. W. Chang, X. Ren, Y. Ao, *et al.*, "Inverse design and demonstration of an ultracompact broadband dual-mode 3 dB power splitter," Opt. Express **26**, 24135–24144 (2018).
31. Z. Yu, H. Cui, and X. Sun, "Genetically optimized on-chip wideband ultracompact reflectors and Fabry–Perot cavities," Photonics Res. **5**, B15–B19 (2017).
32. G. H. Ahn, K. Y. Yang, R. Trivedi, *et al.*, "Photonic inverse design of on-chip microresonators," ACS Photonics **9**, 1875–1881 (2022).
33. N. V. Sapra, D. Vercruysse, L. Su, *et al.*, "Inverse design and demonstration of broadband grating couplers," IEEE J. Sel. Top. Quantum Electron. **25**, 1–7 (2019).
34. C. Dory, D. Vercruysse, K. Y. Yang, *et al.*, "Inverse-designed diamond photonics," Nat. Commun. **10**, 3309 (2019).
35. L. Lu, M. Zhang, F. Zhou, *et al.*, "Inverse-designed ultra-compact star-crossings based on PhC-like subwavelength structures for optical intercross connect," Opt. Express **25**, 18355–18364 (2017).
36. P. Xu, Y. Zhang, S. Zhang, *et al.*, "Scaling and cascading compact metamaterial photonic waveguide filter blocks," Opt. Lett. **45**, 4072–4075 (2020).
37. B. Shen, R. Polson, and R. Menon, "Integrated digital metamaterials enables ultra-compact optical diodes," Opt. Express **23**, 10847–10855 (2015).
38. S. A. Mann, H. Goh, and A. Alu, "Inverse design of nonlinear polaritonic metasurfaces for second harmonic generation," ACS Photonics **10**, 993–1000 (2023).
39. N. Yu, P. Genevet, M. A. Kats, *et al.*, "Light propagation with phase discontinuities: generalized laws of reflection and refraction," Science **334**, 333–337 (2011).
40. J. B. Schneider and K. Abdijalilov, "Analytic field propagation TFSF boundary for FDTD problems involving planar interfaces: PECs, TE, and TM," IEEE Trans. Antennas Propag. **54**, 2531–2542 (2006).
41. J. Jian, P. Xu, H. Chen, *et al.*, "High-efficiency hybrid amorphous silicon grating couplers for sub-micron-sized lithium niobate waveguides," Opt. Express **26**, 29651–29658 (2018).
42. L. Cai and G. Piazza, "Low-loss chirped grating for vertical light coupling in lithium niobate on insulator," J. Opt. **21**, 065801 (2019).
43. I. Krasnokutska, R. J. Chapman, J.-L. J. Tambasco, *et al.*, "High coupling efficiency grating couplers on lithium niobate on insulator," Opt. Express **27**, 17681–17685 (2019).
44. S. Kang, R. Zhang, Z. Hao, *et al.*, "High-efficiency chirped grating couplers on lithium niobate on insulator," Opt. Lett. **45**, 6651–6654 (2020).
45. Y. Liu, X. Huang, Z. Li, *et al.*, "Efficient grating couplers on a thin film lithium niobate–silicon rich nitride hybrid platform," Opt. Lett. **45**, 6847–6850 (2020).
46. Z. Ruan, J. Hu, Y. Xue, *et al.*, "Metal based grating coupler on a thin-film lithium niobate waveguide," Opt. Express **28**, 35615–35621 (2020).
47. E. Lomonte, F. Lenzini, and W. H. Pernice, "Efficient self-imaging grating couplers on a lithium-niobate-on-insulator platform at near-visible and telecom wavelengths," Opt. Express **29**, 20205–20216 (2021).
48. X. Han, Y. Jiang, A. Frigg, *et al.*, "Single-step etched grating couplers for silicon nitride loaded lithium niobate on insulator platform," APL Photonics **6**, 086108 (2021).
49. B. Chen, Z. Ruan, X. Fan, *et al.*, "Low-loss fiber grating coupler on thin film lithium niobate platform," APL Photonics **7**, 076103 (2022).
50. S. Kang, F. Gao, X. Yu, *et al.*, "Lithium niobate thin film grating couplers optimized by particle swarm optimization and a neural network," J. Opt. Soc. Am. B **40**, D21–D25 (2023).
51. X. Zhou, Y. Xue, F. Ye, *et al.*, "High coupling efficiency waveguide grating couplers on lithium niobate," Opt. Lett. **48**, 3267–3270 (2023).
52. X. He, D. Sun, J. Chen, *et al.*, "Inverse designed grating coupler with low loss and high bandwidth on LNOI platform," IEEE Photonics J. **16**, 1–5 (2024).
53. Y. Xie, M. Nie, and S. W. Huang, "Inverse-designed broadband low-loss grating coupler on thick lithium-niobate-on-insulator platform," Appl. Phys. Lett. **124**, 051108 (2024).